Dynamic mesoscale model of the metamagnetic transition in low-bandwidth perovskite manganites

J. Tikkanen,* H. Huhtinen, and P. Paturi
Wihuri Physical Laboratory, Department of Physics and Astronomy, University of Turku, FI-20014 Turku, Finland
(Received 27 January 2017; revised manuscript received 24 April 2017; published 5 July 2017)

Using bulk magnetometry, it was experimentally verified that the metamagnetic insulator-to-metal transition observed in the perovskite manganite $Pr_{1-x}Ca_xMnO_3$ (PCMO) occurs at different critical values of the magnetic-field strength, depending on the macroscopic geometry of the sample in the absence of applied elastic strain. In dimensionally confined samples, such as nanoparticles and thin films, the critical magnetic field can be lower than in bulk by several teslas. To gain a practical understanding of the mechanism behind this correlation, a phenomenological mesoscale simulation was developed to model and analyze the magnetic hysteresis of PCMO. It could be concluded that the low-dimensional samples have a well-defined, permanent free energy bias towards ferromagnetism, something the largely antiferromagnetic bulk all but lacks. The metamagnetic transition field of PCMO turns out to be globally minimized when no external elastic strain is applied and the smallest spatial dimension of the sample approaches 100 nm. The result is likely to apply equally to other low-bandwidth manganites.

DOI: 10.1103/PhysRevB.96.014405

I. INTRODUCTION

The perovskite-structured oxide families $L_{1-x}Ca_xMnO_3$, with $L \in \{Pr,Nd,Sm,Eu,Gd\}$, are often referred to as low-bandwidth manganites, emphasizing the fact that their Mn $3d$ e_g electron band, as calculated within the framework of the double-exchange model, is relatively narrow among manganites [1–3]. Characteristically, these materials are antiferromagnetic (AFM) insulators or semiconductors in their ground state [4,5].

What makes low-bandwidth manganites really stand out among all complex oxide materials is their ability to exhibit the so-called colossal magnetoresistance (CMR) effect near half-doping, $x \approx 0.5$ [6,7]. The family $Pr_{1-x}Ca_xMnO_3$ (PCMO) is particularly famous for this trait, essentially capable of switching from a completely insulating electronic state to a metallic one upon the application of a sufficiently strong magnetic field (of order $\mu_0 H \approx 20$ T, depending on the temperature and Ca doping) [8,9]. Moreover, due to the exquisite correlations between the spin, the charge, and the lattice degrees of freedom of the perovskite manganite structure [1,4,10,11], the CMR effect can be biased using a variety of physical stimuli such as an external electric field, optical illumination, and hydrostatic pressure, shifting the threshold magnetic field required for the insulator-to-metal transition (IMT) by several teslas [12–18].

Such a brilliant IMT, with a resistivity ratio of order 10^7 or higher [18], would naturally be of immediate technological interest (e.g., for sensor applications, contactless switches) should one learn how to tune its occurrence towards room temperature (from below ca. 250 K) [8] and lower magnetic fields (from above 5 T) [8]. As the simple double-exchange model is not enough to explain the scale of the CMR effect [1], a model based on a phase separation into two types of microscopic regions, one type metallic and the other insulating, has been proposed and qualitatively verified [1,7,16,19].

The insulating phase has been attributed to real-space charge and orbital ordering (CO and OO) in the presence of strong cooperative Jahn-Teller distortion, which favors charge localization via the formation of polarons [1,7,14]. The phase is observed to establish a (distorted) AFM order of the CE type [20,21] below ca. 150 K [5]. The metallic phase, on the other hand, shows transport characteristics consistent with the double-exchange model [1,2] and becomes ferromagnetic (FM) below a critical temperature indistinguishable from that of the AFM phase. Even though such a sharp partition into two phases may be an oversimplification and the transitions between these two can actually be more gradual [14,22], the interpretation of the sudden IMT as a percolation of the metallic phase remains prevalent [1,18,23,24].

The present work was largely motivated by the recent discovery that, in addition to optimizing the chemical composition [8,25], the critical magnetic field of the IMT observed in PCMO $x = 0.4$ could be brought down from over 10 T to as low as 2 T at the temperature of 10 K by preparing the samples in the shape of thin films [18,26]. A similar phenomenon has been reported with nanoparticles of $La_{0.25}Ca_{0.25}MnO_3$ compared to their microcrystalline bulk counterpart, explained as an effect of uncompensated surface spins that disrupt the AFM order of the insulating phase in favor of the FM metallic phase [22]. As most of our technological interest lies in the metamagnetic nature of the IMT seen in PCMO [18], the focus of the present paper is to expand on the previous work by developing a phenomenological dynamic micromagnetic model capable of quantitatively reproducing the experimental magnetic hysteresis loops of bulk, nanoparticle, and film samples of PCMO alike.

Very convincing simulations have already been employed to explain the microscopic origin of the magnetic phase separation in manganites, particularly illuminating the role of periodic lattice distortions [7,27]. In contrast, our aims are more towards explaining the macroscopic magnetization dynamics in a way that allows a direct comparison versus bulk magnetometry. To our knowledge, no such models have

*jptikk@utu.fi

TABLE I. Basic parameters of the PCMO samples studied in this work: the sample type, Ca concentration (x), smallest spatial dimension (d), chemical purity, and sample identifier code (ID). Numbers in parentheses indicate standard deviations of the least significant digits derived from Rietveld refinement (B4/5 and N4/5) or from the assumption [30] that pulsed laser deposition retains stoichiometry (F4/5). A purity of 100% means that the measured data could be explained without modeling any secondary phases.

Type	x	d (nm)	Purity	ID
Microcrystalline	0.40(1)	500+	100%	B4
Microcrystalline	0.50(1)	500+	100%	B5
Nanocrystalline	0.39(2)	32(1)	76(1)%	N4
Nanocrystalline	0.49(2)	45(2)	80(1)%	N5
Film	0.40(1)	110	100%	F4
Film	0.50(1)	130	100%	F5

been published for low-bandwidth manganites, even though the field of micromagnetic simulations has greatly matured in recent years, especially from the point of view of permanent magnet materials [28]. In comparison, the methods we are about to introduce can even be seen as relatively simplistic.

State-of-the-art *ab initio* methods, mainly based on density functional theory, have also recently reached a point where materials even as complex as PCMO can be meaningfully modeled [19,29]. Unfortunately, however, phase separation scenarios such as the one used to explain the CMR effect in PCMO remain utterly out of the reach of such methods due to the sheer number of atoms required to model the presence of multiple thermodynamic phases (or even multiple clusters resembling [21] different phases) separated in space. Moving up into the mesoscale, we trade the rigor of *ab initio* methods for a great deal of computational simplicity [28,29], allowing us to model the macroscopic magnetization dynamics as a function of the time, magnetic field, and temperature with provisions for the presence of multiple magnetic phases. Along with this, of course, comes a heightened responsibility to show the meaningfulness of such calculations by comparing them with experimental data.

II. MATERIALS AND METHODS

The materials $Pr_{0.6}Ca_{0.4}MnO_3$ (PCMO $x = 0.4$) and $Pr_{0.5}Ca_{0.5}MnO_3$ (PCMO $x = 0.5$) were synthesized in three forms: ceramic bulk, nanocrystalline powder, and single-crystalline film. Each pair of samples was subjected to a suitable adaptation of x-ray diffractometry (XRD) and dc magnetometry to characterize their structural and magnetic properties. The basic properties of the samples and, importantly, the acronyms used to identify them later are listed in Table I.

A. Sample preparation

The bulk samples B4 and B5 were prepared by conventional solid state synthesis methods [31,32]. Analytical-grade $Pr_{12}O_{22}$, $CaCO_3$, and Mn_2O_3 were dried in air at 500 °C for 6 h, weighed on an analytical balance, and mixed in stoichiometric proportions by mortaring. The mixed powders were compacted into pellets of mass 5 g. The pellets were repeatedly fired in air at 1200 °C for 36 h at a time, then mortared, compacted, and fired again until their x-ray diffractograms (measured using a Philips X'Pert Pro diffractometer, Ni-filtered CuK_α radiation) no longer changed in the process. A final sintering with the same schedule parameters was performed under a flow of 100% laser-grade O_2 to approach the nominal oxygen stoichiometry. The final diffractograms, along with the Rietveld fits which were used to verify the compositions (using the MAUD program [33,34]), are shown in Fig. 1. They correspond to stoichiometries of $Pr_{0.60(1)}Ca_{0.40(1)}MnO_3$ and $Pr_{0.50(1)}Ca_{0.50(1)}MnO_3$ for B4 and B5, respectively. The oxygen content could not be verified directly using XRD but is expected to be very close to (or certainly[35] within 0.025 of) the stoichiometric amount.

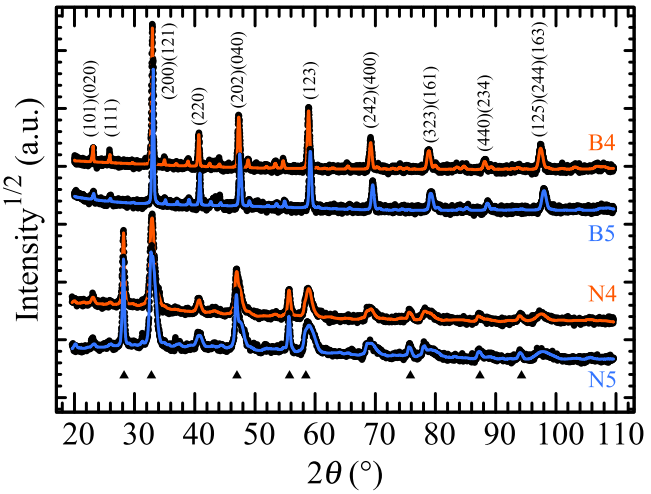

FIG. 1. Room-temperature powder x-ray diffractograms of the bulk and nanoparticle samples. Measured data (small black circles) have been overlaid with the respective Rietveld solutions (solid lines). The major Bragg reflections (of 147 observable) of PCMO have been indexed in accordance with the space group *Pnma*. The triangles at the bottom indicate the most prominent reflections of $Pr_{12}O_{22}$, the sole crystalline impurity phase.

The bulk samples also served the dual purpose of being used as targets for the pulsed laser deposition process of the films. Films were grown on (100) $SrTiO_3$ (STO) single-crystal substrates using a 308-nm XeCl excimer laser under a 30 Pa 100% O_2 atmosphere. The substrate was held at a temperature of 500 °C throughout the growth process and, also, for 10 min afterwards, during which an annealing was performed, with the O_2 pressure increased to 101 kPa. This step would ensure a roughly nominal oxygen stoichiometry in the PCMO lattice. Further details regarding the process can be found in a previous publication [26]. The thicknesses of film samples F4 and F5 were ca. 110 and 130 nm, respectively, as measured by atomic force microscopy across chemically etched ridges.

The phase purity of the films was checked by $\theta - 2\theta$ x-ray diffractograms (Fig. 2) with the film plane kept in the reflection condition. In addition to the Bragg peaks from the sample holder and the STO substrate, only PCMO (0k0) peaks (space group *Pnma*) were identified, indicating that the sole

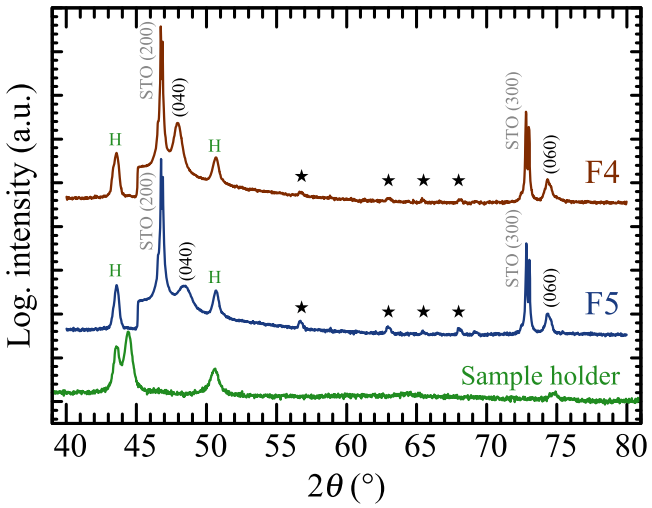

FIG. 2. Room-temperature x-ray diffractograms of the film samples and the bare sample holder assembly. Only the Bragg reflections (040) and (060) are observed from PCMO (space group *Pnma*). Other peaks in the figure originate from the $SrTiO_3$ (STO) substrate (space group $Pm\bar{3}m$), including the star-marked higher order reflections. Reflections from the sample holder are labeled "H." The logarithmic scale strongly emphasizes low-intensity features such as the step below the STO (200) caused by the Ni filter.

crystalline phase on the substrate was PCMO, deposited with its **b** crystal axis normal to the substrate plane as expected [26].

The nanoparticles (samples N4 and N5) were produced by a citrate gel autocombustion method. Stoichiometric amounts of dried $Pr_{12}O_{22}$, $CaCO_3$, MnO_2, and citric acid monohydrate, $C_3H_5O(COOH)_3 \cdot H_2O$ (all of analytical grade), were dissolved in 65% $HNO_{3\,(aq)}$. The amount of citric acid was equal to the total amount of metal cations, i.e., $n(C_3H_5O(COOH)_3 \cdot H_2O) = n(Pr) + n(Ca) + n(Mn)$. To speed up the dissolution, a 50-cm^3 batch of the mixture was placed on a hot plate (300 °C) and continuously agitated by magnetic stirring. Within 15 min the mixture started to clear up, releasing a large amount of gaseous nitrogen oxides and becoming an orange solution.

Fifteen minutes after complete dissolution, as judged by eye based on the transparency, the heat was turned off and the solution was diluted to 1:2 with water. The pH value was adjusted to 5 using $NH_{3\,(aq)}$ and universal indicator paper (a higher pH would cause precipitation), turning the solution green and, finally, pale yellow in color. An amount of ethylene glycol, $C_2H_4(OH)_2$, equal to $4n(C_3H_5O(COOH)_3 \cdot H_2O)$ was added to aid in gel formation. To form a gel, the solution was left on a hot plate (200 °C) for 3 days.

The dry gel, rich in nitrates and organic compounds, is a subsonic explosive with an autoignition temperature between 220 °C and 500 °C. Its deflagration produces large amounts of toxic nitrogen oxide gas, so the calcination of the gel should be done in small batches (10–15 cm^3) and with proper ventilation. We used an open-top vertical furnace heated to 500 °C, allowing 5 min of calcination per sample batch. The gel was carefully mortared prior to the calcination to ensure homogeneous packing.

To crystallize the mostly amorphous combustion products, they were submitted to a 6-h heat treatment in air at 700 °C. Unfortunately, based on XRD and Rietveld refinement (Fig. 1), $Pr_{12}O_{22}$ crystallized almost as readily as PCMO at this temperature, so the initial purity of the PCMO nanoparticles was only about 75%–80%. The purity was observed to improve substantially upon further heat treatment at higher temperatures, reaching 99% after 12 h at 1200 °C, but by this time the crystallite size had also grown close to 1000 nm, defeating the purpose of the synthesis, which was to produce nanoparticles. Since the magnetic behavior of $Pr_{12}O_{22}$ is trivial (paramagnetic; see inset in Fig. 5) and no other secondary phases had crystallized after the initial heat treatment at 700 °C, we chose not to process the nanoparticles any further than this to minimize the crystallite size. The average diameter of the PCMO particles thus obtained was 34 ± 3 nm by the Scherrer equation [36]. Rietveld refinement within the space group *Pnma* showed the stoichiometries to be $Pr_{0.61(2)}Ca_{0.39(2)}MnO_{3-\delta}$ and $Pr_{0.51(2)}Ca_{0.49(2)}MnO_{3-\delta}$ in samples N4 and N5, respectively. Again, the oxygen content could not be verified. Because no final oxygen sintering could be performed without compromising the particle size, a worst-case oxygen understoichiometry of $\delta \approx 0.04$ (equivalent to decreasing x by 0.08) remains possible [35].

B. Sample characterization

After the initial phase purity checks, the XRD studies were extended to lower temperatures using an Anton Paar TTK-450 nonambient chamber with liquid nitrogen cooling. Crystal lattice parameters were determined within the temperature range 83 K $\leqslant T \leqslant$ 403 K at intervals of 40 K. For the bulk and nanoparticle samples this was performed by Rietveld refinement, again using MAUD [33,34]. For the films, individual Levenberg-Marquardt fits to the PCMO Bragg reflections (040), (060), and (103)(301) were made using the STO reflections (200), (300), and (210), respectively, to calibrate the 2θ zero point. The WINPLOTR tool from the FULLPROF program suite [37] was employed for this task.

The magnetizations, M, of the samples were measured as functions of the temperature, T, and magnetizing field, H using Quantum Design MPMS SQUID and PPMS ACMS open circuit dc magnetometers. The $M(T)$ curves were taken at 10 K $\leqslant T \leqslant$ 400 K at temperature intervals of 1.5 K in a field-cooled cooling sequence. Powder samples B4/5 and N4/5 were measured under applied magnetic fields of $\mu_0 H_{ext} = 1$ T, 2 T, . . . , 5 T. Due to the overwhelming diamagnetism of the STO substrate, F4/5 were only measured at $\mu_0 H_{ext} =$ 50, 100, and 150 mT. All of these magnetic fields had been observed to exceed the maximum coercivities of the samples ($\mu_0 H_c \leqslant 20$ mT).

The $M(H)$ hysteresis loops of samples B4/5 and N4/5 were measured up to $\mu_0 H_{ext} = 8$ T on the PPMS. For F4/5, the resolution of the SQUID was required and the maximum field was limited to $\mu_0 H_{ext} = 5$ T by the equipment. The demagnetization factors, N, were roughly fixed by rolling the specimens into balls of PTFE tape or into Al foil. Based on the curve fitting procedure described in Sec. II C the two preparation methods regularly led to $N \approx 0.32 \pm 0.03$ (PTFE)

and $N \approx 0.24 \pm 0.3$ (Al foil), respectively, consistent with the Al foil specimens' being typically somewhat oblong in shape.

C. Simulations

A phenomenological computational model was developed to draw a connection between the proposed nanoscale magnetic phase separation scheme [7] and the observed magnetic hysteresis of PCMO. We assume that an observed $M(H)$ loop is always the superposition of a number of idealized loops, each of which corresponds to a specific energy bias, E_{AFM}, between the FM and the AFM phases and thus, also, to a specific metamagnetic transition (MMT) field, $\mu_0 H_{\mathrm{MMT}}$ [8,9,26]. Our objective is to decompose each observed loop to these spectral components to facilitate a deeper analysis and classification of the magnetization dynamics. In the present work, the resulting spectra were utilized to illuminate the dependence of the energy barrier separating the AFM and FM phases according to the sample geometry.

The micromagnetic simulation responsible for constructing the idealized loops is essentially a metropolis Monte Carlo implementation [38–41] of the exchange spring model [42] on a two-dimensional (2D) triangle lattice. A disk-shaped sample of magnetic clusters is simulated with the clusters confined to the lattice points. The primary ingredient which allows metamagnetic transitions to be modeled is that each cluster can be either FM or AFM in character and can change its character over time in order to minimize the free energy. The FM clusters interact via the standard 2D Heisenberg Hamiltonian,

$$\mathcal{H}_{\mathrm{H}} = -\sum_{i}^{N_{\mathrm{tot}}} \sum_{j}^{N_{\mathrm{n.n.}}} J_{ij}\, \mathbf{S}_i \cdot \mathbf{S}_j - \mathbf{B}_{\mathrm{ext}} \cdot \mathbf{S}_i . \tag{1}$$

Here i indexes every cluster in the simulated sample, the total number of clusters being N_{tot}, and j indexes the nearest neighbors of cluster i, up to $N_{\mathrm{n.n.}}$. In our work, due to the geometry, $N_{\mathrm{n.n.}} \leqslant 6$. $\mathbf{S}_i$ is the magnetic moment of cluster i and $J_{ij} \equiv J$ the exchange coupling between cluster i and cluster j. $\mathbf{B}_{\mathrm{ext}}$ is the external magnetic field.

AFM clusters, on the other hand, are given a constant energy bias, E_{AFM}. This is one of the two parameters of the simulation, the other one being the simulated temperature, T_{sim}. The latter plays its role via the Metropolis proposals [38], stating the probability, $\mathcal{P}$, of any state transition with the associated energy change ΔE:

$$\mathcal{P}(T_{\mathrm{sim}}, \Delta E) = \exp\left(-\frac{\Delta E}{k T_{\mathrm{sim}}}\right). \tag{2}$$

Here k is a unit conversion factor similar to the Boltzmann constant. In our implementation, ΔE is the change in the total free energy that would occur upon the proposed change of state.

Figure 3 showcases the essential features of the simulated system: making E_{AFM} more negative increases $\mu_0 H_{\mathrm{MMT}}$ and decreases the magnetic transition temperature monotonously. In the limit $E_{\mathrm{AFM}} \to -\infty$, no magnetization is possible (the system is totally AFM) and at $E \geqslant 0$ the model reverts to the ordinary 2D Heisenberg model with only FM clusters.

The simulated and observed $M(H)$ data are fitted together using a least squares optimizer [43,44]. The observed data

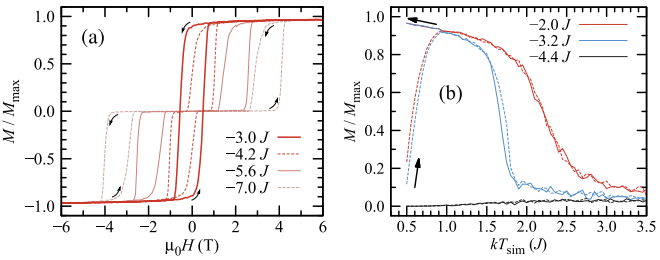

FIG. 3. Simulated data at $kT_{\mathrm{sim}} = 1.0$ J [see Eqs. (1) and (2)]. (a) Simulated normalized hysteresis loops at different constant E_{AFM} values and $kT_{\mathrm{sim}} = 1.0$ J. As E_{AFM} is decreased from −3.0 J (innermost loop; no MMT) to −7.0 J (largest MMT fields), the hysteresis loop splits into two separate subloops along the H axis, with metamagnetic transitions associated with each subloop. Arrows indicate the direction in which the loops are traced over time. (b) Simulated $M(T)$ curves at various E_{AFM} values and $\mu_0 H_{\mathrm{ext}} = 0.5$ T. Both zero-field-cooled (dashed lines) and field-cooled (solid lines) data are shown. Again, arrows indicate the tracing direction. At $E_{\mathrm{AFM}} = -2.0$ J the model is almost fully FM and behaves like an ordinary 2D Heisenberg ferromagnet, but when the AFM component is given a stronger bias, the ordering transition becomes steeper and shifts towards lower T_{sim} until the FM state is totally destabilized. The correspondence with experimental $M(T)$ curves is limited due to the omission of nonhysteretic contributions.

are normalized via the scaling of the magnetization axis, the demagnetization factor, and the linear background slope. Simultaneously, the same algorithm is used to perform the inverse operation of $M(H)$ loop superposition, yielding the spectrum of relative cluster concentrations vs E_{AFM}. The source codes of both the micromagnetic simulation and the data refinement tool are provided in the Supplemental Material [45].

III. RESULTS

For a quick structural overview, the crystallographic unit cell volumes of the bulk and nanoparticle samples (space groups $P2_1/m$ and $Pnma$, respectively) are presented in Fig. 4. The Bragg reflections from the nanocrystals are significantly broadened [36], increasing the error margin in comparison with the bulk data. Unfortunately, the XRD statistics obtained from the films with very little diffracting material were even worse, resulting in standard deviations, σ, of several $\mathrm{\AA}^3$ for the cell volumes. Based on individual lattice parameters measured with a higher resolution at room temperature, however, it could be said that the structure of the films had relaxed as opposed to having remained strained, as would be expected of such relatively thick films [26].

For all three types of samples, the difference in x was clearly manifested in that the 1σ error margins of the cell volume curves at $x = 0.4$ and $x = 0.5$ did not overlap. Additionally, one can see in Fig. 4 that the average volumetric thermal expansion coefficients, γ, of N4/5 are higher than those of B4/5, although this difference is barely statistically significant.

Such differences in γ could carry the physically reasonable implication that the long-range OO is less coherent in N4/5 than in B4/5. In the bulk samples, an anomalous thermal expansion effect attributed to the onset of OO has been

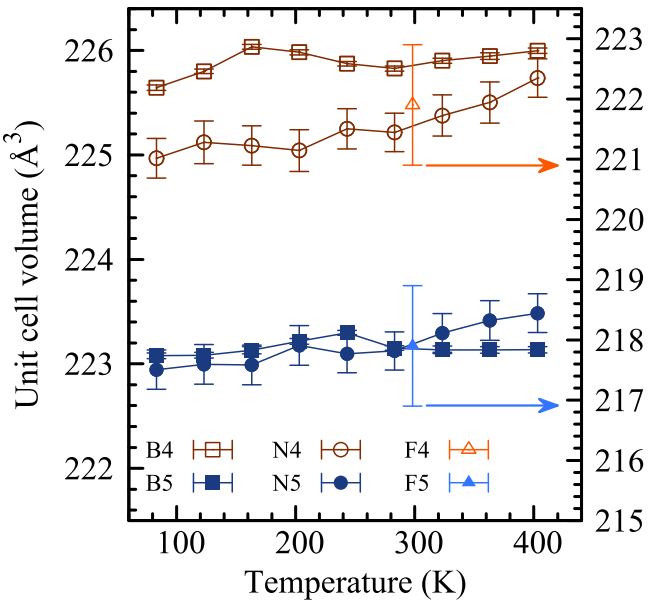

FIG. 4. Crystallographic unit cell volumes of the PCMO samples. Error bars correspond to standard deviations derived from Rietveld refinement (B4/5 and N4/5) or individual Levenberg–Marquardt fits (F4/5). Room-temperature cell volumes of the films are presented on a separate scale (right) to accommodate their large deviation from the polycrystalline samples.

observed to transiently increase the cell volume, decreasing the average thermal expansion coefficient within the corresponding temperature range [46]. That the OO is less coherent in the dimensionally confined samples is corroborated to some extent by the $M(T)$ curves shown in Fig. 5: the magnetic anomaly that accompanies the onset of CO and OO [47–50] at $T \approx 250$ K is much stronger in the bulk samples than in N4/5 or F4/5. It is in fact completely missing from the film data.

Unfortunately, because the magnetic anomaly is not hysteretic, but corresponds to an increase in paramagnetic susceptibility upon the formation of FM chains along the Mn sites in anticipation of the low-temperature CE AFM structure [47–50], it cannot be reproduced by our computational model. On the other hand, the fit against the $M(H)$ curves observed at $T \leqslant 100$ K, below the Néel temperature of the CE AFM system, is very good, as shown in the comparison plot in Fig. 6. Somewhat astonishingly, the shape of the hysteretic part turns out to be almost independent of the Ca concentration, x: only the material mass fraction which produces the hysteretic signal (not shown) is different between samples of the same type. For example, the hysteretic variation in the magnetization of B4 is roughly four times higher than that of B5 [31].

Figure 6(a) also succinctly illustrates our main motivation for this work (see Sec. I). The FM phase resulting from the MMT is much more stable in the dimensionally confined samples F4/5 and N4/5 than in B4/5, as demonstrated by the demagnetizing curves being convex in the former set of samples and concave in the latter. Also, crucially, the point of maximum curvature on the magnetizing curve, which can be identified as the critical field of the MMT, $\mu_0 H_{\mathrm{MMT}}$ [26], in the absence of resistive measurements [18], is observed to depend on the sample geometry. For example, the $\mu_0 H_{\mathrm{MMT}}$ points can

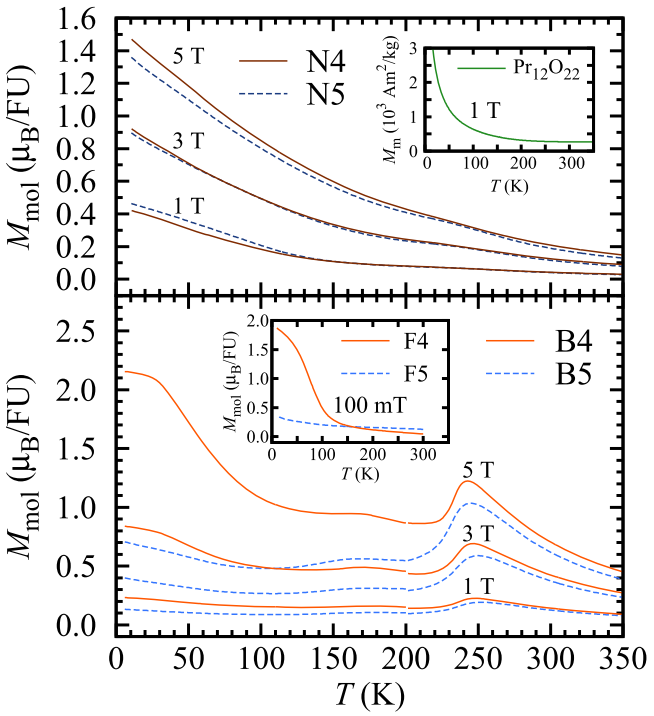

FIG. 5. Molar magnetizations of the polycrystalline samples as functions of the temperature, $M(T)$. The applied external magnetic fields (1, 3, and 5 T for N4/5 and B4/5; 100 mT for F4/5) are indicated next to each pair of curves. There is a discontinuity in the bulk sample data at $T = 200$ K due to the simultaneous measurement on two magnetometers. These curves have been matched at $\mu_0 H_{\mathrm{ext}} = 5$ T by tuning the demagetization factor of the low-T curves; the remaining discrepancies are an effect of the sample history. Systematic errors of order 10% are possible along the magnetization axes due to uncertainties in the demagnetization factors. Upper inset: Paramagnetic $M(T)$ curve (in terms of the specific magnetic moment) of the impurity phase $Pr_{12}O_{22}$. Though found among N4/5, the magnetization of $Pr_{12}O_{22}$ is too small to be seen in the main panel. Lower inset:$M(T)$ curves of the film samples.

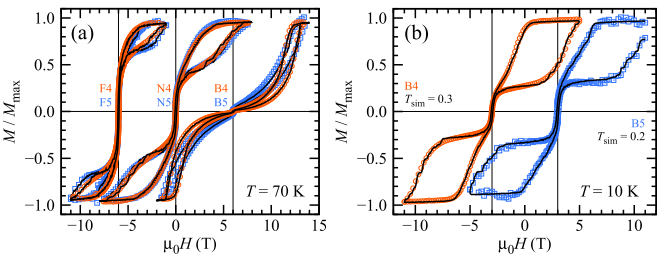

FIG. 6. (a) Normalized magnetic hysteresis loops of all samples at $T = 70$ K. Data at the Ca concentration $x = 0.5$ have been overlaid with data at $x = 0.4$. The origins of the loops have been shifted for clarity. Open small circles and open squares represent measured data ($x = 0.4$ and $x = 0.5$, respectively); solid black lines, simulated data. The form of the loops is qualitatively almost independent of x but varies strongly between samples of different geometry. (b) The same as (a), for B4/5 at 10 K. The basis set used in the spectral decomposition appears reasonable: even the incomplete closure of the B5 curve is modeled correctly.

be found ca. 3, 4, and 5 T away from the origin in F4, N4, and B4, respectively. At $x = 0.5$, the differences between F5 and N5 are smaller, but the $\mu_0 H_{\mathrm{MMT}}$ of these is still lower than that of B5 by roughly 1 T.

Overall, no single calibration transform could be established between the simulated and the real temperatures, but a specific one was needed for each sample. Furthermore, N4/5 and F4/5 were well modeled within $T_{\mathrm{sim}} \leqslant 0.7$ J, whereas $T_{\mathrm{sim}} = 1.6$ was required to explain the 100 K behavior of B4/5. These findings signal a significant difference in the AFM-FM equilibration rates between different sample geometries, the bulk samples being much quicker to adjust their magnetic phase equilibrium.

The refined distributions of the bias energies of the AFM state, $n(E_{\mathrm{AFM}})$, have been collected in Fig. 7 for samples B4/5 and N4/5. The spectra of F4/5 were qualitatively similar to those of N4/5 but are omitted for brevity and due to their low signal-to-noise ratio. Some aliasing between neighboring E_{AFM} channels is visible, suggesting that a lower channel density might have been sufficient for the fits. It is evident based on the high weights at $E_{\mathrm{AFM}} = -8$ J that the maximum magnetic field of 8 T used in the measurements was not enough to explore all physically possible MMT fields. Indeed, fields in excess of 20 T would reportedly be needed for this [8,9].

One can see in Fig. 7 that more regions of the energy landscape become available for the MMT when the temperature is increased, but the pattern in which the regions become active drastically depends on the sample geometry. The dimensionally confined samples N4/5 show a clear cutoff energy (roughly −5 J) below which $n(E_{\mathrm{AFM}})$ uniformly increases with the temperature. In the bulk samples, no such cutoff is present, but the $n(E_{\mathrm{AFM}})$ weight spreads gradually towards higher E_{AFM} when the temperature is increased. Note that the basis set of simulated loops into which the experimental data are decomposed (and thus the mapping

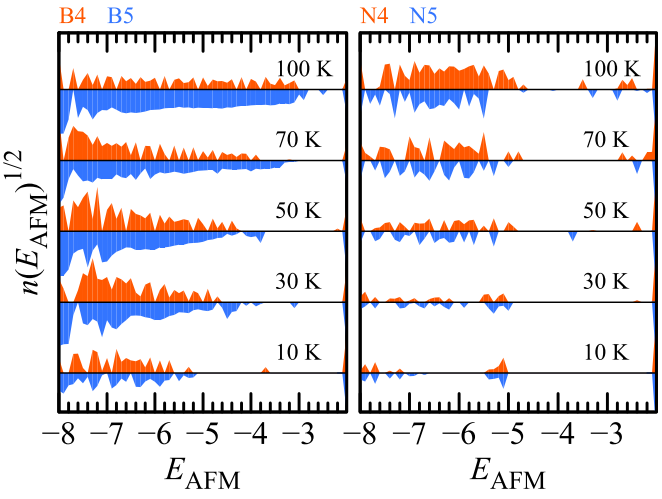

FIG. 7. $n(E_{\mathrm{AFM}})$ spectra of the bulk and nanocrystalline samples. More regions of the energy landscape become available for the MMT when the temperature is increased, but the pattern of this over the E_{AFM} axis greatly depends on the sample geometry. Evidently, the maximum magnetic field of 8 T used in the measurements was not enough to explore all physically possible MMT fields.

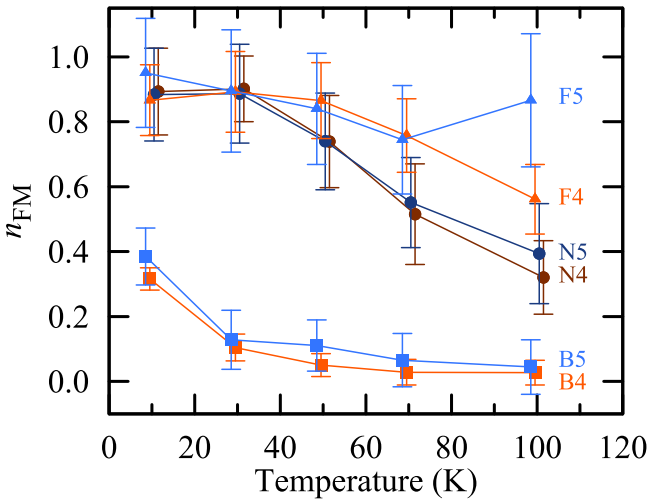

FIG. 8. Relative concentrations of permanently FM hysteretic clusters in each sample, n_{FM}, as functions of the temperature. Errors correspond to maximal parameter shifts when the square error of the underlying fits is allowed to increase by 1%. Curves have been shifted slightly along T to help distinguish individual error bars.

between $\mu_0 H_{\mathrm{MMT}}$ and E_{AFM}) depends on the temperature, so comparisons between B4/5 and N4/5 in Fig. 7 are only straightforward at a given temperature.

To visualize the effect of sample geometry even better, we have extracted the relative concentrations of permanently FM clusters, n_{FM}, from each spectrum and plotted these versus the real temperature in Fig. 8. The difference between the dimensionally confined samples and the bulk is evident.

IV. DISCUSSION

It is important to note that all of our samples were essentially free of elastic strain, except perhaps for the very surface of the nanoparticles and the film-substrate interfaces. Strain has been shown both experimentally and theoretically to be a major factor determining the magnetic phase equilibrium in manganites [24,27], so we were well off minimizing this additional complication. In fact, about 100 nm appears to be the optimal thickness of PCMO films for minimizing the $\mu_0 H_{\mathrm{MMT}}$, below which substrate-induced strain begins to play a role and can actually shift the magnetic properties back closer to the bulk performance [51]. Incidentally, this length scale also coincides with the optimum reported for $La_{0.25}Ca_{0.25}MnO_3$ nanoparticles with an e_g bandwidth slightly larger than that of PCMO [22]. It seems plausible that when the smallest dimension of a manganite sample approaches 100 nm, the coherence distance of the glassy surface spin states and the relaxation of any surface strain quite universally form something of a perfect balance for minimizing the $\mu_0 H_{\mathrm{MMT}}$.

Our present results (see, e.g., Fig. 8) verify a larger persistent FM contribution in the dimensionally confined samples in conjunction with the lowered $\mu_0 H_{\mathrm{MMT}}$ values. Moreover, the spectral decompositions shown in Fig. 7 provide an explanation for the mechanism behind this correlation: whereas the bulk samples show a relatively broad distribution of energy barriers that must be overcome for the MMT to occur, the dimensionally confined samples are statically biased by the

surface spins so that the low-energy MMTs ($E_{\mathrm{AFM}} \geqslant -5\,J$) have, in a sense, "already happened," and the energetically deeper regions can be switched with a correspondingly smaller applied field.

Our model was developed for manganites capable of undergoing metamagnetic AFM–FM transitions. This mainly limits its applicability to low bandwidth manganites near half doping, $x \approx 0.5$ [7,21], although evidence of similar magnetization dynamics has also arisen at lower hole concentrations, at $x \approx 0.1$ [19,52,53]. For FM high bandwidth manganites the model simply reverts to a 2D Heisenberg ferromagnet, providing little physical information for the effort.

At $x \approx 0.5$, low bandwidth manganites like PCMO exhibit a complex interplay between the elastic, electronic and magnetic degrees of freedom: the two first are mainly coupled via the Jahn-Teller mechanism, whereas the double exchange mechanism connects the last two [1,4,54]. Our model does not consider the free energy contributions from each degree of freedom individually, but they are implicitly summed up to the empirically determined E_{AFM} values. This can be seen as both a weakness and a strength, and it is clear that further work is in order to strengthen the applicability and interpretation of the model. In particular, the micromagnetic simulation could rather easily be extended to support a resistor network model of the full CMR effect.

V. CONCLUSIONS

We have experimentally verified that the MMT observed in approximately half-doped PCMO occurs at different values of the magnetic field strength, $\mu_0 H_{\mathrm{MMT}}$, depending on the macroscopic geometry of the sample even in the absence of externally generated elastic strain. In dimensionally confined samples such as nanoparticles and thin films the critical magnetic field can be lower than in bulk PCMO by several teslas. In previous literature, this effect has been attributed to a glasslike FM phase being generated at the crystal interfaces of nanoparticles, working as a nucleation source for the metallic FM phase, which dominates over an insulating AFM phase above $\mu_0 H_{\mathrm{MMT}}$. We have now generalized this result to films and, arguably, any other geometries with a comparable fraction of surface area over volume.

To transfer the results from nanoparticles to films, a simplistic but quantitatively accurate phenomenological simulation model was developed for analyzing the $M(H)$ hysteresis loops of PCMO. A specialized spectral decomposition of the loops gave a clear picture of the mechanism behind the reduction of $\mu_0 H_{\mathrm{MMT}}$ in the dimensionally confined samples: these have a clear cutoff energy difference between the FM and the AFM phases, with regions above the cutoff permanently locked in the FM phase. In the bulk samples, on the other hand, an applied magnetic field must convert a wider spectral range of regions into the FM state before the MMT can occur, explaining the higher $\mu_0 H_{\mathrm{MMT}}$.

All in all, even though applied elastic strain perhaps remains the most effective tool for tailoring the magnetofunctional properties of manganites [24,27], we can conclude that the geometry itself may also be utilized to fine-tune the critical field of the MMT. In particular, there appears to be a characteristic length of ca. 100 nm, a "sweet spot" of sorts, at which the coherence distance of the glassy surface spin states and the relaxation of any surface strain form a perfect balance with the bulklike periodic lattice modulations to minimize the $\mu_0 H_{\mathrm{MMT}}$ [22]. In the case of PCMO, and possibly other closely related manganites as well, we observe that the global minimum of $\mu_0 H_{\mathrm{MMT}}$ is in fact attained at any given temperature (where the MMT is possible) when no external elastic strain is applied and the smallest sample dimension approaches 100 nm.

ACKNOWLEDGMENTS

The authors wish to thank the Jenny and Antti Wihuri Foundation, Finland, for financial support. J.T. also acknowledges the University of Turku Graduate School for general resources and finance.

[1] M. B. Salamon and M. Jaime, Rev. Mod. Phys. **73**, 583 (2001).
[2] J. Fontcuberta, B. Martínez, A. Seffar, S. Piñol, J. L. García-Muñoz, and X. Obradors, Phys. Rev. Lett. **76**, 1122 (1996).
[3] N. Biškup, A. de Andrés, I. M. Ochando, and M. T. Casais, Phys. Rev. B **73**, 184404 (2006).
[4] J. Coey, M. Viret, and S. von Molnár, Adv. Phys. **58**, 571 (2009).
[5] Z. Jirák, S. Krupička, Z. Šimša, M. Dlouhá, and S. Vratislav, J. Magn. Magn. Mater. **53**, 153 (1985).
[6] Y. Tokura and Y. Tomioka, J. Magn. Magn. Mater. **200**, 1 (1999).
[7] E. Dagotto, T. Hotta, and A. Moreo, Phys. Rep. **344**, 1 (2001).
[8] M. Tokunaga, N. Miura, Y. Tomioka, and Y. Tokura, Phys. Rev. B **57**, 5259 (1998).
[9] M. Respaud, A. Llobet, C. Frontera, C. Ritter, J. M. Broto, H. Rakoto, M. Goiran, and J. L. García-Muñoz, Phys. Rev. B **61**, 9014 (2000).
[10] D. Efremov, J. van den Brink, and D. Khomskii, Nat. Mater. **3**, 853 (2004).
[11] G. Milward, M. Calderon, and P. Littlewood, Nature **433**, 607 (2005).
[12] A. Asamitsu, Y. Tomioka, H. Kuwahara, and Y. Tokura, Nature **388**, 50 (1997).
[13] H. Yoshizawa, H. Kawano, Y. Tomioka, and Y. Tokura, Phys. Rev. B **52**, R13145(R) (1995).
[14] P. Beaud, A. Caviezel, S. O. Mariager, L. Rettig, G. Ingold, C. Dornes, S.-W. Huang, J. A. Johnson, M. Radovic, T. Huber, T. Kubacka, A. Ferrer, H. T. Lemke, M. Chollet, D. Zhu, J. M. Glownia, M. Sikorski, A. Robert, H. Wadati, M. Nakamura, M. Kawasaki, Y. Tokura, S. L. Johnson, and U. Staub, Nat. Mater. **13**, 923 (2014).
[15] S. Majumdar, T. Elovaara, H. Huhtinen, S. Granroth, and P. Paturi, J. Appl. Phys. **113**, 063906 (2013).
[16] D. E. Cox, P. G. Radaelli, M. Marezio, and S.-W. Cheong, Phys. Rev. B **57**, 3305 (1998).
[17] M. C. Langner, S. Zhou, G. Coslovich, Y.-D. Chuang, Y. Zhu, J. S. Robinson, W. F. Schlotter, J. J. Turner, M. P. Minitti,

R. G. Moore, W. S. Lee, D. H. Lu, D. Doering, P. Denes, Y. Tomioka, Y. Tokura, R. A. Kaindl, and R. W. Schoenlein, Phys. Rev. B **92**, 155148 (2015).
[18] T. Elovaara, S. Majumdar, H. Huhtinen, and P. Paturi, Adv. Funct. Mater. **25**, 5030 (2015).
[19] J. Tikkanen, M. Geilhufe, M. Frontzek, W. Hergert, A. Ernst, P. Paturi, and L. Udby, J. Phys.: Condens. Matter **28**, 036001 (2016).
[20] E. Wollan and W. Koehler, Phys. Rev. **100**, 545 (1955).
[21] E. Dagotto, *Nanoscale Phase Separation and Colossal Magnetoresistance: The Physics of Manganites and Related Compounds* (Springer Science & Business Media, New York, 2013), Vol. 136.
[22] T. Zhang, T. F. Zhou, T. Qian, and X. G. Li, Phys. Rev. B **76**, 174415 (2007).
[23] M. Uehara, S. Mori, C. H. Chen, and S.-W. Cheong, Nature **399**, 560 (1999).
[24] K. Lai, M. Nakamura, W. Kundhikanjana, M. Kawasaki, Y. Tokura, M. Kelly, and Z.-X. Shen, Science **329**, 190 (2010).
[25] C. Martin, A. Maignan, M. Hervieu, and B. Raveau, Phys. Rev. B **60**, 12191 (1999).
[26] T. Elovaara, T. Ahlqvist, S. Majumdar, H. Huhtinen, and P. Paturi, J. Magn. Magn. Mater. **381**, 194 (2015).
[27] K. H. Ahn, T. Lookman, and A. R. Bishop, Nature **428**, 401 (2004).
[28] J. Fidler and T. Schrefl, J. Phys. D: Appl. Phys. **33**, R135 (2000).
[29] H. Ebert, D. Ködderitzsch, and J. Minár, Rep. Prog. Phys. **74**, 096501 (2011).
[30] G. Subramanyam, M. Cole, N. Sun, T. Kalkur, N. Sbrockey, G. Tompa, X. Guo, C. Chen, S. Alpay, G. A. Rossetti Jr., K. Dayal, L.-Q. Chen, and D. Schlom, J. Appl. Phys. **114**, 191301 (2013).
[31] T. Elovaara, H. Huhtinen, S. Majumdar, and P. Paturi, J. Phys.: Condens. Matter **24**, 216002 (2012).
[32] J. Tikkanen, H. Huhtinen, and P. Paturi, J. Alloys Compd. **635**, 41 (2015).
[33] L. Lutterotti, MAUD: Materials Analysis Using Diffraction, 2.71 (http://maud.radiographema.com, 2016)
[34] L. Lutterotti, M. Bortolotti, G. Ischia, I. Lonardelli, and H. Wenk, Z. Kristallogr. Suppl. **26**, 125 (2007).
[35] E. Pollert, S. Krupička, and E. Kuzmičová, J. Phys. Chem. Solids **43**, 1137 (1982).
[36] A. Patterson, Phys. Rev. **56**, 978 (1939).
[37] J. Rodríguez-Carvajal, Physica B **192**, 55 (1993).
[38] W. K. Hastings, Biometrika **57**, 97 (1970).
[39] C. Robert and G. Casella, *Monte Carlo Statistical Methods* (Springer-Verlag, New York, 2004).
[40] S. Kirkpatrick, C. Gelatt, and M. Vecchi, Science **220**, 671 (1983).
[41] H. Anderson, Los Alamos Sci. **14**, 96 (1986).
[42] E. Kneller and R. Hawig, IEEE Trans. Magn. **27**, 3588 (1991).
[43] E. Jones, T. Oliphant, P. Peterson *et al.*, SciPy: Open source scientific tools for Python, (2001–); https://www.scipy.org/
[44] D. Kraft *et al.*, *A Software Package for Sequential Quadratic Programming* (DFVLR, Oberpfaffeuhofen, Germany, 1988).
[45] See Supplemental Material at http://link.aps.org/supplemental/10.1103/PhysRevB.96.014405 for the source codes of the micromagnetic simulation and the data refinement tool (in C++ and PYTHON, respectively).
[46] J. Tikkanen, S. Kauhala, H. Huhtinen, and P. Paturi, Phys. Procedia **75**, 475 (2015).
[47] H. Yang, Y. Liu, J. Zhang, X. Zhang, Z. Cheng, Y. Xie, B. Wang, Q. Zhan, B. G. Shen, E. W. Plummer, and R.-W. Li, Phys. Rev. B **91**, 174405 (2015).
[48] M. R. Lees, J. Barratt, G. Balakrishnan, D. M. Paul, and M. Yethiraj, Phys. Rev. B **52**, R14303(R) (1995).
[49] N. Biškup, A. de Andrés, and M. G. Hernández, Phys. Rev. B **78**, 184435 (2008).
[50] K. Okada and S. Yamada, Phys. Rev. B **86**, 064430 (2012).
[51] T. Elovaara, H. Huhtinen, S. Majumdar, and P. Paturi, Appl. Surface Sci. **381**, 17 (2016); e-MRS Fall Meeting 2015, Symposium L: Towards oxide-based electronics: Growth and applications of oxide thin films and heterostructures.
[52] H. Gamari-Seale, I. Troyanchuk, D. Khalyavin, K. Stefanopoulos, and J. Hernández-Velasco, Physica B: Condens. Matter **350**, E19 (2004).
[53] I. Troyanchuk, S. Pastushonok, O. Novitskii, and V. Pavlov, J. Magn. Magn. Mater. **124**, 55 (1993).
[54] C. Moure and O. Peña, Prog. Solid State Chem. **43**, 123 (2015).